

Experimental confirmation of secondary flows within granular media

Received: 20 September 2024

Accepted: 24 July 2025

Published online: 26 August 2025

 Check for updates

Andres Escobar ^{1,2}, James Baker ³, François Guillard ², Thierry Faug ¹ & Itai Einav ² 

As collections of grains flow, free-surface deformations often develop. These typically suggest the presence of secondary flows, smaller in magnitude than the primary motion but driving complex three-dimensional internal structures. While one can infer such behaviour from boundaries or simulations, we have not previously been able to directly observe secondary flows experimentally. In this paper we present an experimental confirmation of secondary kinematics within granular media using dynamic x-ray radiography, without needing to stop motion for tomography. Specifically, we create a bulldozing mechanism of conveyor-driven grains. This generates a non-uniform, indented free-surface, hinting that secondary mechanisms are at play alongside the primary regime. Discrete element method simulations are shown to be consistent with this secondary-flow explanation. We then probe further experimentally using two perpendicular x-ray source/detector pairs to measure the velocity inside the bulk. This indeed unveils a complex three-dimensional flow pattern that deviates from the primary vertical planes and must include vortices and convection rolls. This advancement is pertinent for industrial and natural scenarios where grains impact obstacles, and has broader relevance for studying the rheology associated with secondary flows in other amorphous materials such as emulsions, pastes and colloids.

Understanding the complex behaviour of dense amorphous soft materials, ranging from granular materials to emulsions, remains a fundamental challenge in soft matter physics^{1,2}. These materials exhibit intricate flow dynamics that significantly influence their macroscopic properties. This is particularly apparent in granular media^{3,4}, which are ubiquitous in both nature and industry, appearing in forms as diverse as sand, mineral ores, and cereals. The physical description of these materials is challenging due to their propensity to transition between solid-, liquid-, and gaseous-like phases based on external excitation rather than on their thermal temperature. Modelling the fluid-like phase of granular materials is particularly involved when one wishes to take into account the complex interactions with boundaries. For instance, when a geophysical granular flow encounters an abrupt change in topography, or when grains on industrial conveyors impact

an obstacle, the flow can exhibit a sudden change in surface height, known as a shock or discontinuity. It is widely understood that such surface discontinuities conceal complex interactions and displacements beneath the free surface, yet measuring the corresponding internal flow field remains a significant challenge.

A commonly proposed internal flow mechanism in granular systems is ‘secondary flows’. These represent displacements in directions different from the flow’s primary component that are typically smaller in magnitude. For example, grains in a granular avalanche predominantly move in the downslope direction, but there may also be smaller recirculating or convection-like motion in the transverse or normal directions to the slope^{5–7}. Secondary flows are not unique to granular media; they also occur in classical Newtonian fluids such as water⁸, where they are much better understood thanks to the water’s

¹Université Grenoble Alpes, CNRS, INRAE, IRD, Grenoble INP, IGE, Grenoble, France. ²School of Civil Engineering, The University of Sydney, Sydney, NSW, Australia. ³School of Computer Science and Mathematics, Liverpool John Moores University, Liverpool, UK. ✉e-mail: Itai.Einav@sydney.edu.au

transparency, which allows for extensive volumetric observations^{9,10}, often through the use of tracers^{11,12}, and thanks to the well-established rheological properties of water^{13,14}. Our understanding of secondary flows in water currents is crucial, for instance for designing open-channel structures^{15–17} and in fluvial geomorphology^{18,19}.

However, the experimental study of secondary flows in granular media remains challenging due to the opacity of the grains. We often rely on numerical simulations, usually in the form of particle-based discrete element method (DEM) computations. While these provide valuable insights into the internal flow, they only represent a simplified model of the actual physical system. On the other hand, we can make experimental observations at either the free surface or lateral sidewalls to deduce the existence of secondary flows. For example, Forterre and Pouliquen made surface velocity and thickness measurements to infer the existence of longitudinal vortices²⁰, which accurately matched the results of a linear stability analysis²¹. However, boundaries are known to alter the flow itself due to the formation of granular boundary layers^{22,23}, and therefore, such measurements do not provide the full internal picture. There have been some experimental studies of secondary flows in granular suspensions using refractive-index-matched particles submerged in viscous fluids^{24,25}. However, in these regimes, the development of secondary flows cannot be attributed purely to granular effects, as similar flows inevitably occur in pure fluids¹².

The experimental study of secondary flows underneath the free surface of dry granular media requires advanced imaging techniques capable of seeing through the bulk of opaque grains. One such method is magnetic resonance imaging (MRI), which has been used to effectively measure internal particle velocities in continuously flowing Couette geometries²⁶ but has not previously detected the existence of secondary flows. X-ray computed tomography (CT) is another non-invasive method that constructs a three-dimensional (3D) density map from which grain locations can be retrieved. This technique works by successively capturing x-ray radiographs from multiple directions, which requires intermittent pauses between flow periods to accommodate the extended time needed to obtain such radiographs without grain motion and imaging artifacts^{27–29}. For this reason, most research on secondary flows in dry granular media focuses on quasi-static conditions, such as those achieved using a Couette cell^{30–36}. While much can be learned from this approach, the majority of natural and industrial granular flows are continuously moving, which presents a fundamentally different deformation regime that is never left to relax to a static state. Up until now, investigations of secondary flows in continuous flow configurations have been limited to DEM simulations or inferred from experimental observations at boundaries.

Here, we advance the experimental investigation of the development of secondary flows in continuously flowing granular media. This is done without requiring interstitial fluid or intermittent halting of motion for volumetric measurements. Similarly, the methods presented here can be applied to any form of granular media – whether dry, saturated, or partially saturated – as well as to general heterogeneous flowing media, such as foams and active matter. The particular laboratory setup consists of a bulldozed granular flow in an open channel, which is established by driving grains from the base using a rubber conveyor belt and colliding these with a perpendicular wall. This creates a non-uniform free surface, known as a heap^{37,38}. Crucially, the flow is significantly faster than in the Couette cell geometry previously used to investigate secondary flows. Similar conveyor-belt-driven configurations have previously been used to examine strain localisation at sidewalls using optical particle image velocimetry (PIV)³⁹. Here, we instead use fast x-ray radiography from two perpendicular positions and develop a measurement technique to study the 3D shape of the strongly deformed free surface. This suggests the presence of secondary flows beneath the free-surface, which we explore with DEM models. We then experimentally measure the 3D velocity field along the main flow direction using x-ray rheography⁴⁰.

When combined with velocity fields averaged across both the width and the height of the flow, this provides a robust experimental volumetric observation of secondary flows in continuously flowing granular media.

Results

The experimental setup giving rise to secondary flows is sketched in Fig. 1. The configuration is an open flume positioned above a conveyor belt, imaged through two x-ray radiography systems. The flume has a reservoir of grains at one end, and a wall suspended with a gap from the conveyor belt at the other. An initial pile of grains is carried by the conveyor belt and forms a heap upon reaching the suspended wall. This heap stabilises when the effect of its weight on the outgoing flow under the wall balances the incoming flow from the emptying reservoir. According to the inertial numbers analysed in the Supplementary Information, the granular flow is largely faster than the quasi-static regime but slower than the collisional regime. High-speed x-ray radiography is then employed to analyse the heap, enabling the investigation of internal flow dynamics within the granular media, with reduced influence from the sidewalls on the images. Radiographs are obtained during motion from two perpendicular directions: vertically through the conveyor (*z* direction), and horizontally through the lateral sidewalls (*y* direction). Panels (a) and (b) in Fig. 1 show example radiographs obtained for the corresponding two x-ray detectors. Note that a third detector parallel to the *x* direction is not considered as the x-ray beam would have to pass through the full length of the chute and reservoir, which would attenuate the signal too much to make meaningful measurements. Supplementary Video 1 is also available online, showing the two sets of dynamic radiographs alongside the physical experimental setup. A DEM simulation is also conducted that complements the experimental flow observations. Technical details of this simulation and of the experimental setup and procedures are described in the Methods section. While the results section focuses on a single set of parameters, the robustness of the findings is further illustrated for other values in the Supplementary Information.

Experimental 3D surface elevation profiles

The granular flow was first analysed by developing an x-ray image reconstruction method with which the 3D details of the deformed free surface along the heap were measured, as shown in Fig. 2a. The key idea is to use the time-averaged intensity fields from one x-ray direction to estimate the absorption coefficient of the material in the other direction. The technical details of this reconstruction process are described in the Methods section.

After the heap has fully stabilised in the flume, it exhibits a relatively uniform appearance across the width. Surprisingly, however, the reconstruction also reveals a pronounced dip at the start of the heap. This can be seen in the 2D height profiles at different positions, depicted in Fig. 2b. Note that there are also smaller fluctuations in the free-surface profile that are attributed to the discrete, granular nature of the material. These are not fully smoothed out when averaging the x-ray intensity over time, especially at the slower-moving section near the wall. Note also that the height profile displays a minor overall slope across the width, which is also apparent in the supplementary tests. This is attributed to x-ray scattering or to the conical shape of the x-ray beam, leading to uneven illuminating intensity in *y*.

Secondary flows in DEM simulations

In light of past research revealing secondary flows under non-uniform free surfaces^{30,32–34,41}, the dip at the start of the heap raises the question of whether such flow might develop beneath the bulldozed grains. In this scenario, the primary flow moves along the *x* direction, as it is primarily driven by the belt, and in the normal *z* direction, as the development of a heap necessitates particles climbing upwards to conserve mass, irrespective of secondary flows. Conversely, any bulk

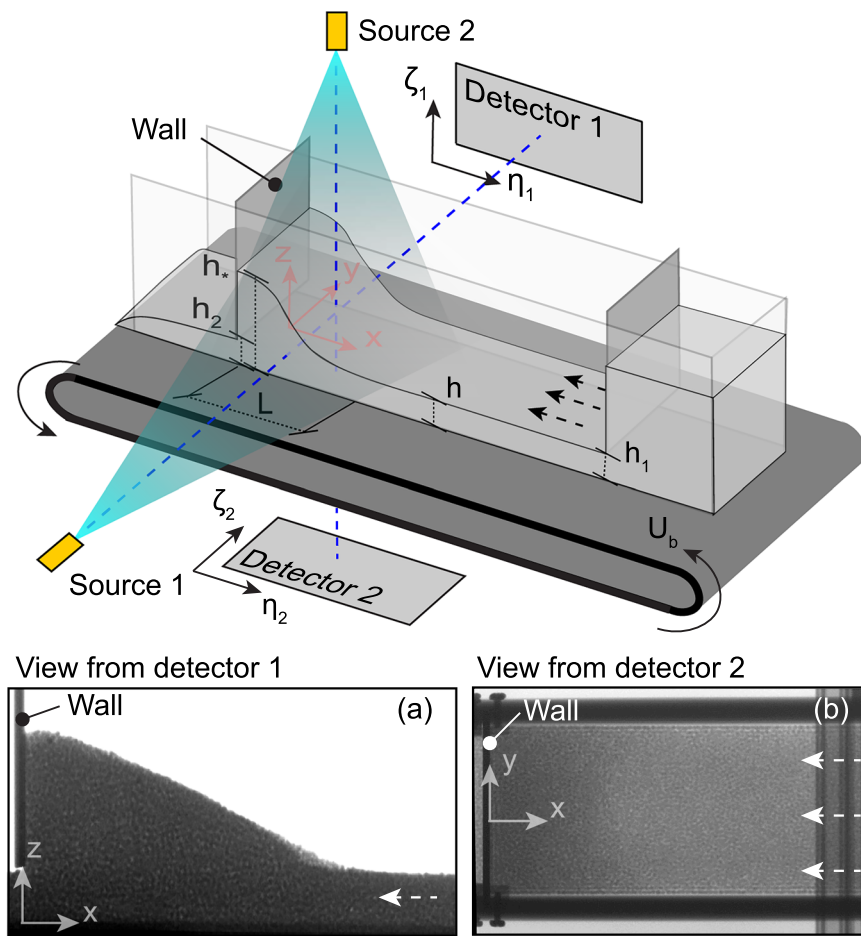


Fig. 1 | Experimental setup showing the conveyor-driven flow and the position of the x-ray imaging setup. Here, h is the flow thickness, L the heap length, and h its height. The wall at the exit of the reservoir and the outgoing wall are elevated at heights h_1 and h_2 , respectively, which control the steadiness of the heap. The conveyor belt moves at a velocity U_b in a counter-clockwise direction, as indicated by the circular arrows at the edges of the belt. The conveyor belt transports the

particles in the direction indicated by the dashed arrows. **a** and **b** show example radiographs captured during the steady state for detectors 1 and 2, respectively. The origin of the global coordinate system (x, y, z) is at the centre of the line connecting the wall and the conveyor belt. Coordinate systems (η, ζ) are local to each x-ray detector. The experimental geometry and radiographs are illustrated using Supplementary Video 1 (available online).

motion in the transverse y direction should be attributed directly to secondary flows, as this direction is orthogonal to the main stream of material.

To investigate the possibility of secondary flow, we thus focus on the coherent existence of velocities along the y direction. We begin by developing a DEM simulation, which is designed to replicate the experiment. The technical details of the simulation are described in the Methods section.

The DEM simulation was first used to evaluate the free-surface x-ray measurement technique described in full in the Methods section. To achieve this, the free surface in the DEM simulation was analysed using both its coarse-grained density field (Fig. 2c) and the same x-ray technique applied to synthetic radiographs, which were generated from the DEM model as in previous work⁴⁰ based on particle positions and assumed x-ray attenuation properties (Fig. 2d). The strong agreement between Fig. 2c, d confirms the validity of the free-surface x-ray technique, thereby supporting the experimental findings in Fig. 2a and the existence of the dip at the start of the heap.

Second, the simulation also allowed us to obtain the three velocity components U_x , U_y , and U_z parallel to their respective axes through the flow. Following the visualisation method proposed by Krishnaraj & Nott³², the coarse-grained field of U_y and the streamlines normal to the belt motion are shown in Fig. 3 in order to highlight secondary flows. Indeed, the U_y velocity field and the cross-sectional streamlines display

strong evidence of secondary flows. This is particularly visible through cross-section 3b around the dip at the start of the heap. The cross-sectional streamlines at this position reveal a flow directed upwards, displacing horizontally from the walls towards the centre. The secondary flows are around one order of magnitude smaller than the basal velocity U_b driving the primary flow at this position.

Moreover, the secondary flows are not constrained to only this position. Figure 3a reveals that the incoming flow before the heap also displays secondary flows, this time even smaller at around three orders of magnitude below U_b . These weak secondary flows are in the form of small rollers near both lateral walls, rotating inwards toward the centre of the flume. Elsewhere at this x position, the flow established by the DEM model is influenced predominantly by the conveyor belt with minimal vertical or transverse displacements ($U_y \approx 0$, $U_z \approx 0$), and hence the streamlines in Fig. 3a display more incoherent patterns.

The secondary flow is also weaker after the dip vanishes, as illustrated in cross-section 3c, where the free-surface becomes more uniform along the width of the flume. Here, there is only a weak signal of secondary flow, again in the form of convection rollers near the lateral boundaries. However, the corresponding motion changes direction again, now heading outwards from the centre towards the walls. Supplementary Video 2 (available online) illustrates the emergence and disappearance of these different phenomena when moving along the flume in the x direction.

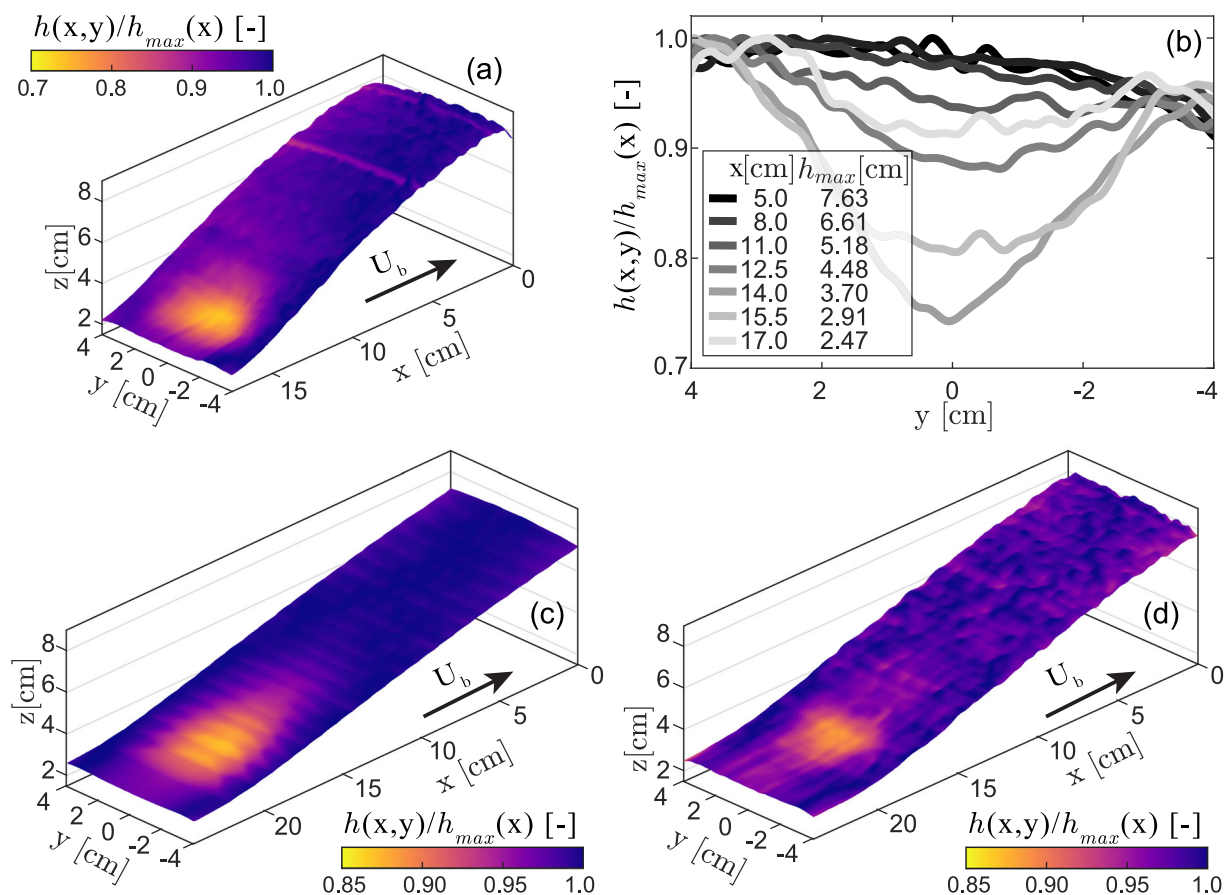


Fig. 2 | Free surface of the flowing granular media in both the experiment and the discrete element method (DEM) simulation. **a** and **b** show the experimental free surface and relative height profiles at various x -positions, respectively. **c** and **d** display the free surface in the DEM simulation using coarse-grained density field

and synthetic radiographs, respectively. The different colours in the three free-surface plots represent the relative heights at each given x -axis position ($h(x, y)/h_{max}(x)$). The arrows indicate the direction of the conveyor belt velocity (U_b).

3D velocity field from x-ray rheography

Having obtained strong evidence of secondary flows in the DEM simulations, we now return to the experimental configuration to establish whether we can detect similar secondary flows in the physical system. Rather than the free-surface profile already obtained using the x-ray reconstruction method, attention is now shifted to the velocity fields, specifically the internal flow field.

A 3D reconstruction of the U_x velocity field was obtained using the two perpendicular sets of radiographs and the x-ray rheography technique developed by Baker et al.⁴⁰, with the results shown on Fig. 4a. The undisturbed flow, before the heap, was found to move at velocity U_b with no slip at the bottom at the centre of the flume, demonstrating a well-controlled conveyed flow set-up. The presence of the sidewalls, however, induces some shearing across the width with velocities decreasing toward the walls. In the heap, two different layers are observed parallel to the x -axis, producing a horizontal band of shearing through the height, emanating from around the height of the incoming flow h_1 . Below $-h_1$, the average velocity of the flow is slightly below U_b . The thickness of this horizontal shear band appears to be influenced by the heap's weight. Above $-h_1$, the flow shows little motion.

The DEM result of the U_x velocity field seen in Fig. 4b accurately replicates the main features of the rheography result, including the velocity variation along the width of the channel, and the presence of the horizontal shear band. The interaction between the heap and the flow underneath also appears similar to the results from the numerical

simulation of Sauret et al.³⁷ (referring specifically to their figure 18 (a)). One notable difference between the x-ray experiments and the DEM results is the slope of the heap. Despite both tests producing similar heap height, h , the experiment exhibits a shorter heap length compared to the DEM result. However, the qualitative evolution of the U_x velocity field is similar to the one obtained from the experimental x-ray rheography, suggesting that should secondary flow also exist in the physical reality, it would not influence the main flow direction.

Experimental confirmation of secondary flows through the depth of granular media

In addition to the 3D reconstruction of the U_x velocity component, we apply correlation-based particle image velocimetry (PIV) analysis of the two sets of radiographs to obtain U_y and U_z velocity fields, depth-averaged in the direction of the x-ray beams²³. This complementary imaging method provides insight into all velocity components, which strongly consolidate our finding of secondary granular flows in the experimental setup. For the purpose of cross-validation, these analyses were conducted on both real experimental radiographs and simulated radiographs, the latter based on particle positions from DEM and assumed x-ray attenuation properties. Technical details are available in the Methods section.

Figure 5 displays the contours of the depth-averaged velocity fields from both the experimental and simulated radiographs. The U_x velocity fields present multiple similarities, as displayed in Fig. 5a, b, e, f, consistent with Fig. 4. When viewed from above using detector 2 (see

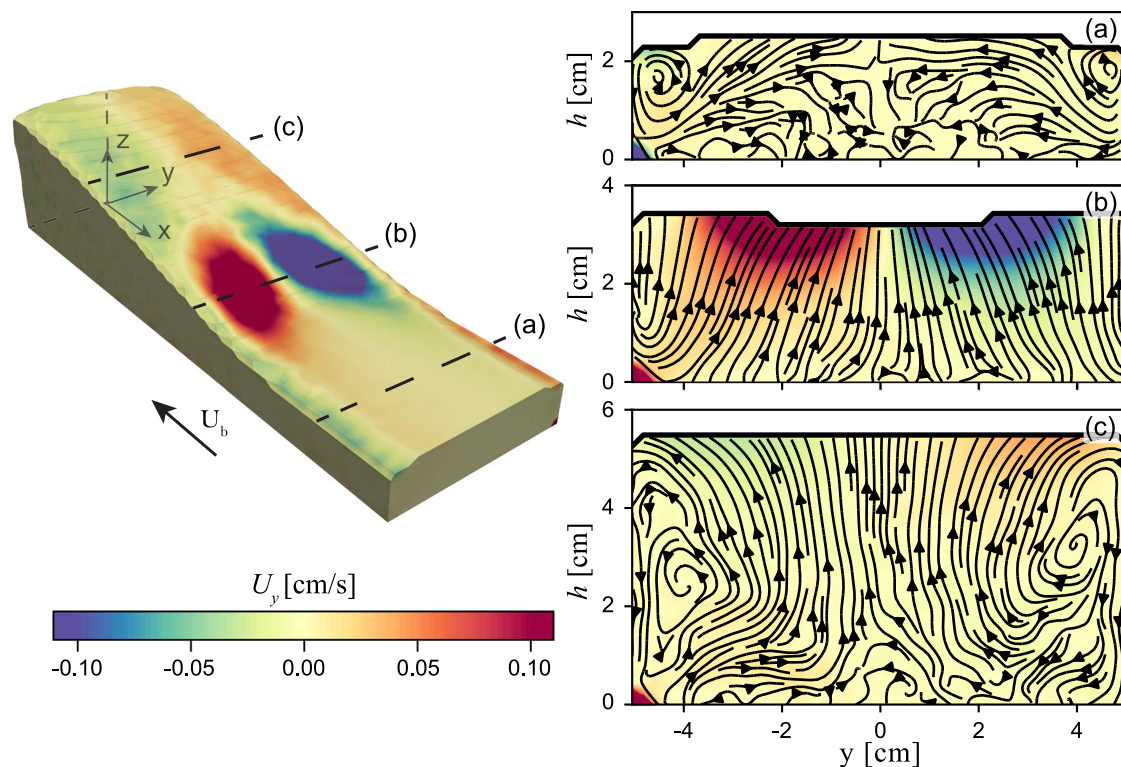


Fig. 3 | Secondary flow field of velocity component from the discrete element method simulation. Left plot shows the value of the horizontal (U_y) velocities at the surface of the flow. Here, the arrow indicates the direction of the conveyor belt velocity (U_b). **a–c** show the value of U_y on three different slices along the flume at

$x_a = 41.8$ cm, $x_b = 34.1$ cm, $x_c = 20.5$ cm from the exit wall, respectively, as well as cross-sectional streamlines of U_y and the vertical (U_z) velocities. Supplementary Video 2 (available online) shows the U_y velocity component and the cross-sectional streamlines along the x -axis.

Fig. 5a, b), both the experiment and simulation show an incoming flow at the centre of the flume that follows the conveyor velocity. The velocity gradually decreases when moving towards the heap, as well as when moving from the centre toward the walls. When viewed from the side using detector 1 (see Fig. 5e, f) both cases show a similar shear band between the bottom of the flow and the heap, where the lower material flows at velocities close to U_b . Above the shear band, the flow develops very slowly. The DEM simulation accurately reproduces the observed shear band.

More importantly, as depicted from the top view of detector 2 by both the experiment and simulation in Fig. 5c, d, respectively, the horizontal velocity component U_y reveals distinct secondary flows at the start of the heap, which move from the walls toward the centre. All velocities in Fig. 5 are normalised by the belt velocity U_b , allowing easy comparison of the corresponding magnitudes. This indeed confirms that the secondary flow is significantly slower than the primary conveying motion, being an order of magnitude less than U_b . As the dip vanishes, the secondary flow shifts direction, moving from the centre of the flume toward the walls. This transition is more prominent in the experimental velocity field in Fig. 5c, implying potential issues of replicating the exact boundary conditions and particle interactions in the DEM simulation.

Side-view analysis from detector 1 of the U_z vertical velocity fields in Fig. 5g, h shows a robust upward flow where the free surface starts to ascend, with higher magnitude in DEM simulations compared to the experiments. In addition, a pronounced downward flow is observed near the outgoing gate, influenced by the exit wall. The area of this downward flow is more extensive in the DEM results.

Note that, in general, x-ray rheography can be applied to recover the full three components of velocity in three dimensions⁴⁰. However, this requires three mutually perpendicular imaging direction. For this

particular experimental setup, this would involve positioning an x-ray source and detector along the x -direction, meaning the beam would have to pass through the full length of the chute and reservoir. This would have caused excessive attenuation, making it virtually impossible to measure the components U_y and U_z in 3D. Nevertheless, the 3D measurements of U_x , combined with the depth-averaged values for the other components, support the secondary flow observations.

Discussion

This paper has presented experimental confirmation of a secondary flow within the bulk of continuously moving granular media. Using a confined chute and conveyor belt to establish a bulldozing mechanism, we are able to probe the system through a variety of x-ray radiography techniques and establish the presence of secondary vortices within the dry granular bulk. These techniques enable such secondary flows to be internally measured experimentally without having to artificially change the system (e.g., restricting to quasi-static motion, as in CT) or change the material (e.g., add viscous interstitial fluid, as in refractive index matching scanning).

Note that several methods exist to estimate grain velocities along the surface of a granular bulk, and these measurements have previously been used to infer secondary flow within the material^{20,21}. However, in general, two significant limitations exist from such a surface measurement approach. First, surface velocity measurements must carefully account for and exclude the effects of particles seeping into or emerging from the bulk. Second, and more critically, surface measurements alone cannot provide conclusive insights into the flow within the bulk because surface particles represent only a negligible fraction of the total particles in the system. In fact, visual inspection of our system has revealed surface disturbances in the form of localised and often gaseous backward-avalanching

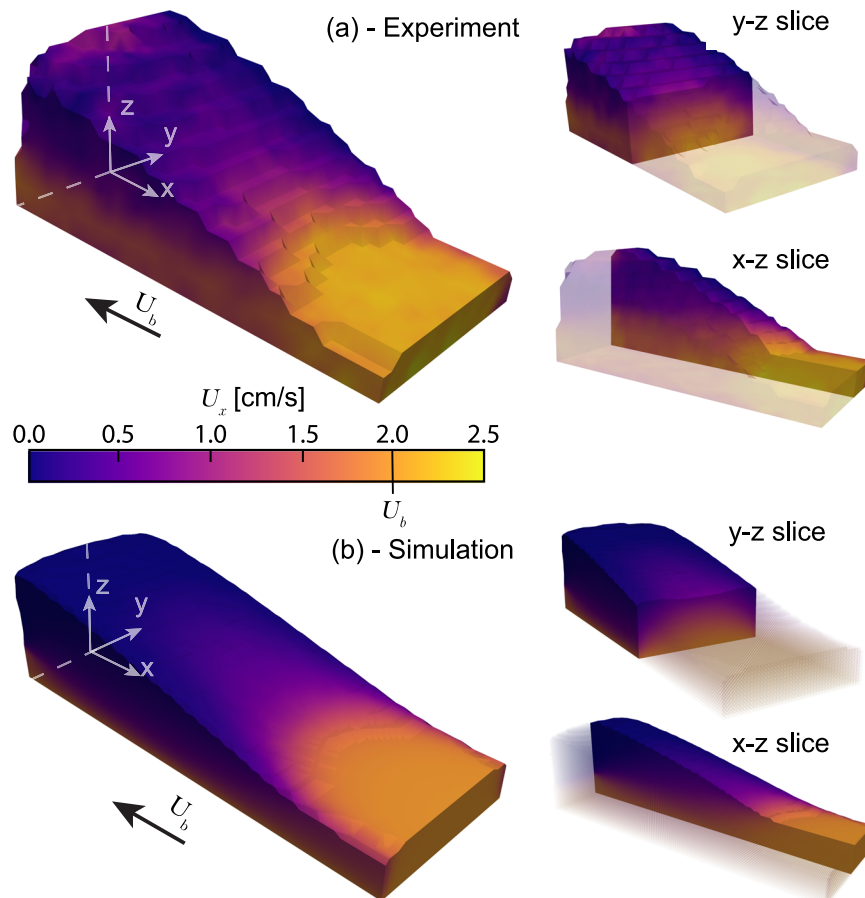


Fig. 4 | Cross-validation of the x-ray experiments and numerical simulations. The x -axis velocity fields (U_x) derived through the experimental x-ray rheography technique and the discrete element method simulations are shown in **a** and **b**,

respectively, with additional slice views in $y-z$ and $x-z$ planes. The arrows indicate the direction of the conveyor velocity (U_b), which moves from right to left in all panels.

surface-grains that, in isolation, would mislead conclusions about the flow within the bulk. Similarly, bulk quantities such as depth-averaged velocities are not necessarily related to boundary or surface measurements. For example, in the rotating cylinder system previously investigated by Baker & Einav⁴², positive and negative displacements cancel each other out, making the beam-averaged velocity equal to zero. However, just measuring from the sidewall of the cylinder (if it was made of transparent material) would suggest all lateral velocities are non-zero and moving in the same direction. In contrast, the method proposed in this article directly addresses these limitations by considering the flow of all grains throughout the thickness or depth of the bulk, rather than focusing solely on surface particles. As such, the results presented here offer an experimental validation of secondary flow within the bulk of continuously moving granular media.

In establishing the presence of secondary flows in this system, we have developed an x-ray methodology for measuring the 3D surface profile of flowing granular media. This could be useful beyond the specific geometry and material investigated here, for example where the free surface is obstructed by airborne grains or rigid structures making optical imaging difficult but where x-rays could still be transmitted through. We have also applied existing dynamic x-ray radiography²³ and rheography⁴⁰ methods to a new geometry, further strengthening the value of these tools both in isolation and, crucially, in conjunction with each other and the free-surface measurements to build a more complete picture of the secondary flows. A further methodological innovation is the use of

dynamic x-ray radiography to measure depth-averaged velocities. While the same approach has previously been applied to compute quantities averaged in the lateral directions (avoiding sidewall effects)²³, depth-averaged quantities are of particular interest because they can be compared directly to shallow-water type flow models. These models have been particularly pivotal in studying geomorphological changes caused by soil erosion and landslides, as well as glacial landforms and snow avalanches^{43–45}. Combining the x-ray method for 3D free surface profiling with the application of x-ray radiography for measuring depth-averaged velocities provides a powerful means of comprehensively evaluating the predictions of shallow-water-type models.

The experimental observations made in this paper allow us to investigate the secondary flow patterns and mechanism. To further our understanding of this and other geometries, it is important to isolate the controlling factors that determine the presence and magnitude of such secondary flows. Since the secondary vortices are confined and placed symmetrically between the lateral sidewalls, a key question here is whether these boundaries are required to produce such flow patterns. To this end, we have also studied the dependence of the secondary flows on sidewalls using DEM simulations of a similar configuration but with either frictionless sidewalls or periodic boundary conditions in the lateral directions (see Supplementary Information). In the frictionless sidewall case, some traces of secondary flows could still be detected. On the other hand, the analysis using the periodic boundaries appears to entirely eliminate the secondary flows, suggesting that the boundedness is indeed a

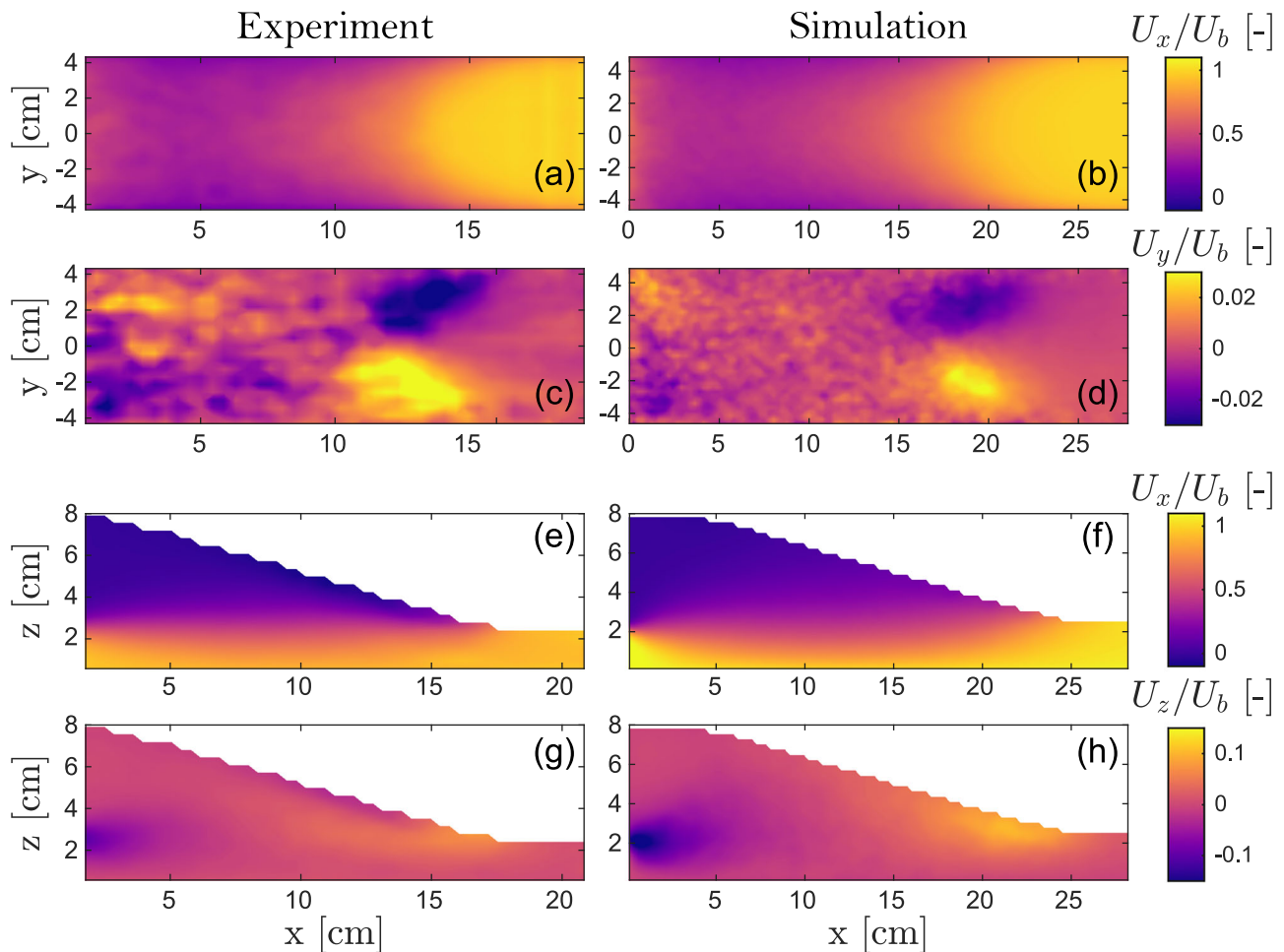


Fig. 5 | Experimental confirmation of secondary flows under bulldozed grains using particle image velocimetry of depth-averaged velocity fields from two orthogonal x-ray radiographs (left column). These results are cross-validated with the corresponding depth-averaged velocity fields of the discrete element method simulation (right column), recreated from artificially generated radiographs. **a** and

b refer to the x -axis velocity fields (U_x) seen from the top (detector 2). Similarly, **c** and **d** display the y -axis velocity fields (U_y). x -axis velocity fields from the side (detector 1) are shown on **e** and **f**, and z -axis velocity fields (U_z) are displayed on **g** and **h**. All velocity fields are normalised by the velocity (U_b) of the conveyor, which transports particles from right to left in all the above panels.

necessary condition and that secondary flows would not form spontaneously in an unconfined setting. A more comprehensive study of the exact role of the wall properties in the development of secondary flows remains open. While most bulldozed grain systems will, in practise, be bounded by the finite domain of the bulldozer cap, this observation helps inform higher-order constitutive models incorporating, for example, non-local effects⁴. These models can, in turn, contribute to our understanding of other potential secondary mechanisms in unbounded flows, such as the presence of longitudinal ridges on Martian landslide deposits⁴⁶, which have been postulated to occur during the transition from thick to thin flow regimes.

Building on the results presented here, future work could apply the same general tools to different materials to investigate, for example, the role of grain shape and convexity, which has previously been found to induce qualitatively distinct secondary mechanisms^{27,30}. Furthermore, the complementary imaging approach, key to the success of this study, could be extended further to allow us to study an even broader range of granular and glassy media. In particular, to elucidate whether the granular or viscous fluid phase drives secondary flows in suspensions, one could combine the dry granular tools presented here with submerged refractive index-matching scanning experiments. This would provide insight into the behaviour of saturated and partially saturated systems.

Methods

Experimental setup

The experimental flume is divided into three sections: a reservoir to supply incoming grains, the flow region of interest, and an outflow region where grains leave the system and fall into a bucket. The length of the flow domain is 0.55 m, and it has a width of 0.10 m. The walls separating these regions are elevated at heights h_1 and h_2 above the belt and the lateral sidewalls. The sidewalls confine the flow for the whole length of the experimental domain, including the outflow. The conveyor belt is made of rubber with uniformly distributed asperities of size 3 mm. The two cross-flow walls and the flume are all made out of 1cm-thick acrylic sheets, whereas the front wall, which accumulates the heap, is made of aluminium. To avoid vibrations during tests, the flume was first pressed against the conveyor belt under its weight and then anchored tightly using beams at the top of the system, out of the line of x-rays. This anchoring approach prevented grains from slipping under the walls or even getting stuck during the tests, thus averting any potential belt damage.

The granular material comprises spherical glass beads with an average diameter of $d = 3$ mm. The test is set up by first filling up the reservoir with grains, as well as placing an additional pile of grains with a height $> h_1$ next to the reservoir gate, inside the flow region of interest. As the belt starts moving, the new grains entering the flowing domain join the pile and eventually either impact the outgoing wall or

flow through the downstream opening, so their aggregated bulk eventually forms a steady heap a few seconds after impact. The online Supplementary Video 1 captures this process. The steady state concludes when the reservoir empties, which ceases the incoming flux and gradually reduces the heap's size until it levels and disappears. Through trial and error it was found that by taking $h_2 = h_1 - d/2$ the flow maintained a sufficiently prolonged steady state geometry for x-ray imaging that lasted up to 2 minutes, limited by the capacity of the reservoir.

Multiple tests were performed, all with the belt velocity U_b fixed at 2 cm s^{-1} to eliminate motion blur on the x-ray radiographs. On the other hand, we varied h_1 from 25 to 60 mm, and the height of the heap h_* from 50 mm to $h_* \approx 100 \text{ mm}$ by changing the initial amount of grains on the conveyor belt. The test results show that the heap length L solely depends on the heap height $h_* - h_l$, and the heap maintains a constant slope $\alpha \approx 18^\circ$. Given this trend, a single test is analysed in this study, with $h_1 \approx 25 \text{ mm}$ and $h_* \approx 77 \text{ mm}$. Additional test results confirming the robustness of the mechanism are presented in the Supplementary Information.

The x-ray sources were positioned -2 m from the flume to minimise non-parallel beam effects. Similarly, the x-ray detectors were situated around 20 cm from the flume in the opposite direction of their respective sources, as depicted in Fig. 1. Steel panels were positioned to prevent undesired illumination of the detectors from their non-associated sources. During tests, the sources were set to produce x-ray at a maximum energy of 190 keV and 4 mA current for source 1, and 190 keV and 5 mA for source 2. Radiographs were captured at a frequency of 30 fps with a resolution of $960 \times 768 \text{ px}$ at 16-bit with a spatial resolution of 0.29 px mm^{-1} and 0.22 px mm^{-1} for detectors 1 and 2, respectively. In addition to the full, flowing system, radiographs were also obtained of the empty chute to aid subsequent analysis. The accuracy of the 2D and 3D velocity measurement methods presented in this work has been studied using known velocity fields^{23,40}. While the methods sometimes introduce quantitative errors, they qualitatively recover a range of underlying fields and therefore the secondary flow findings in this paper are believed to be robust.

Free surface measurement

Here, we introduce a reconstruction method for establishing 3D profiles of free surfaces of granular flows using x-ray radiography from two orthogonal directions. The starting point of the method assumes that the radiograph intensity I_i from the i -th detector follows the Beer-Lambert absorption law⁴⁷:

$$I_i = I_{i,R} \exp\left(-\int \mu(\xi) d\xi\right), \quad (1)$$

where $I_{i,R}$ is the i -th detector's reference intensity of the radiograph of the empty flume, $\mu \equiv \mu(\xi)$ is the local absorption of the material at the ξ location, while the integral is over the x-ray beam length.

In the case of detector 2, assuming that there is no significant spatial change in the volume fraction of the dense flowing material, Eq. (1) simplifies and rearranges to:

$$h_{\text{BL}}(x, y) = -\frac{1}{\mu_c} \ln\left(\frac{I_2(x, y)}{I_{2,R}}\right), \quad (2)$$

where $h_{\text{BL}}(x, y)$ is the theoretical Beer-Lambert surface height profile, and μ_c is the effective material absorption of the grains on detector 2, which is assumed constant. The radiograph intensities I_i , used in this process, are depicted in Supplementary Video 3, along with their values normalised by $I_{i,R}$. In order to capture additional effects such as beam hardening and x-ray scattering, which are not considered by the Beer-Lambert law, we consider the following empirical linear relation

for the actual surface height profile:

$$h(x, y) = -\frac{1}{\mu_c} \left\langle \ln\left(\frac{I_2(x, y)}{I_{2,R}}\right) \right\rangle_t - \frac{\beta_c}{\mu_c}, \quad (3)$$

with β_c a constant.

In order to obtain μ_c and β_c , we first calculate a nominal profile of the averaged height along the y direction, $\langle h \rangle_y \equiv \langle h \rangle_y(x)$ using detector 1. This is done from direct thresholding of the time-averaged absorption field $\langle \ln(I_1/I_{1,R}) \rangle_t$, and is well-defined thanks to the very different absorption of air and grains, and the fact that the material height does not vary much across the y direction of the flume, even near the dip.

To first order, the surface height at the centre of the flume is estimated by $h(x, 0) \approx \langle h \rangle_y$. Then, the effective material attenuation coefficient μ_c on detector 2 can be found by fitting a linear law from the time-averaged absorption field observed at each pixel along the centre line:

$$\left\langle \ln\left(\frac{I_2(x, 0)}{I_{2,R}}\right) \right\rangle_t = -\mu_c h(x, 0) - \beta_c, \quad (4)$$

where we obtain $\mu_c = 0.01117 \text{ mm}^{-1}$, as well as $\beta_c = 0.2304$ which was introduced to allow for additional effects of beam hardening and x-ray scattering. The fit can be seen in Supplementary Fig. 2.

As a last step, $h(x, y)$ from Eq. (3) is smoothed with a 2D Gaussian filter of standard deviation 6 px.

DEM simulations

The physical experiments were computationally modelled using the DEM through the open source code YADE⁴⁸. The simulations involved $N \approx 120,000$ spherical particles, which were modelled using a viscoelastic contact law with a linear spring for normal contacts and a Coulomb threshold for tangential contacts⁴⁹. These particles have the same average diameter $3 \pm 0.75 \text{ mm}$ as the glass beads used in experiments, with some added polydispersity to avoid crystallisation while preventing segregation. Their interparticle friction was set at 0.5, their stiffness at $1 \times 10^7 \text{ Pa}$, their density was set at 2500 kg m^{-3} to mimic the material and ensure maximum interparticle deformation of $10^{-4}d$. The normal restitution coefficient was set at 0.5, and the Poisson's ratio at 0.3. To mimic the geometric effects of the rubber conveyor belt, its texture of was simulated using a set of spheres with a fixed spacing of every two rows along the y -axis, at a height $z = 0$, with a longitudinal row at a height of $z = -d$. These boundary grains were set in motion at velocity U_b and had an increased friction coefficient of 1.0. A similar friction coefficient was set to describe the acrylic walls, aligning with literature values for the friction coefficient between glass with acrylic and rubber⁵⁰. Fictitious rolling friction was not implemented since the boundary spheres provide an actual physical rolling resistance. However, different friction coefficient values and belt arrangements were tested, with the stated combination of parameters above exhibiting the closest similarity to the experimental result while also aligning with the physical properties of the simulated materials.

The experimental setup for the simulations mirrored the physical experiment: a reservoir initially filled with grains and a pile of grains situated inside the flume. The pile height was adjusted to match h_* upon reaching a steady state. Once a constant state was achieved, the grains' locations, velocities, and radii were recorded to a file at a frequency of 30 fps, mirroring the experimental setup. 2700 frames were used for the simulations presented in this work. Next, a coarse-graining method⁵¹ was employed to obtain the velocity and density fields of the recorded flowing spheres, using a Lucy windowing function with a radius of $2d$.

Synthetic radiographs were generated from DEM data as in previous studies^{40,42} using the sphere positions and radii to calculate the

attenuation along the x-ray path. This was based on an idealised system where the sample consists of solid particles, each of the same uniform x-ray attenuation coefficient, and interstitial air of negligible attenuation compared to the solid phase. Assuming a parallel x-ray beam with no scattering, the Beer-Lambert attenuation law then simplifies to

$$I_{DEM} = I_{0,DEM} \exp(-\mu_{DEM}D), \quad (5)$$

where $I_{0,DEM}$ is the initial x-ray intensity before travelling through any grains, μ_{DEM} is the constant attenuation coefficient and D is the total thickness of grains that the x-ray beam travels through. This thickness will depend on the pixel position (η, ζ) in the local imaging coordinates and can be calculated by summing each of the N projected particle thicknesses. For detector 1 the depth is then given by

$$D_1(\eta_1, \zeta_1) = \sum_{i=1}^N 2\sqrt{\max(r_i^2 - (x_i - \eta_1)^2 - (z_i - \zeta_1)^2, 0)}, \quad (6)$$

and similarly for detector 2 the depth is

$$D_2(\eta_2, \zeta_2) = \sum_{i=1}^N 2\sqrt{\max(r_i^2 - (x_i - \eta_2)^2 - (y_i - \zeta_2)^2, 0)}, \quad (7)$$

where (x_i, y_i, z_i) and r_i represent the position and radius of particle i . These two thicknesses are calculated for each frame and Eq. (5) is then used to generate the corresponding artificial radiographs with an arbitrary attenuation coefficient of $\mu_{DEM} = 10$, initial intensity $I_{0,DEM} = 100,000$ and spatial resolution 3 px mm^{-1} .

Velocity reconstruction using x-ray rheography

In order to emphasise the density fluctuations within the flow, the radiographs are first divided by the time-averaged intensity of the steady-state frames $\langle I \rangle_t$. The absorption fluctuation field (μ_{fluct}) is then calculated by

$$\mu_{\text{fluct}} = \ln\left(\frac{I}{\langle I \rangle_t}\right), \quad (8)$$

as depicted in Supplementary Video 3. The 3D velocity field is reconstructed using the x-ray rheography technique⁴⁰ applied to the normalised intensity fields μ_{fluct} . We focus on the x -axis velocity component, which is common to both imaging directions. X-ray rheography is a correlation-based algorithm that first reconstructs the distribution of in-plane displacements through the out-of-plane direction by solving a deconvolution problem⁴². It then solves an optimisation problem to combine velocity distributions from two perpendicular directions and reconstruct internal velocity fields. The accuracy and sources of errors of x-ray rheography have previously been investigated for both the initial distribution reconstruction⁴² and the whole rheography process⁴⁰ (see Supplementary Information within).

Here, we apply the initial correlation analysis on successive pairs of images using an interrogation window size of 32 px and a maximum displacement of ± 16 px. The deconvolution process was conducted utilising regularisation parameters $\alpha = 0.1$ and $p = 2.0$ (see Baker et al.⁴⁰), and this was repeated for multiple pairs of images to improve accuracy, up to a maximum of 100,000 evaluations. The optimisation problem was solved by averaging the best 100 configurations with the smallest errors from a total of 10,000 to give the resulting internal x velocities. Note that this velocity field assumes a uniform free surface across the width of the flume, and thus disregards the obtained dip along with any other variation in the free surface. The calculated velocity fields are therefore trimmed using the free surface measurements in order to eliminate extrapolated velocities out of the granular domain.

PIV analysis of the depth-averaged flows

The experimental depth-averaged velocity fields were computed from successive x-ray radiographs using the methodology developed by Guillard et al.²³ for granular silos, which was validated against known flow rates from a mass balance. PIV analysis was performed on the attenuation fluctuation fields μ_{fluct} from the experiments and the DEM synthetic radiographs using the software PIVLab⁵². For the DEM radiographs, the analysis was conducted using auto contrast, with FFT window deformation as the PIV algorithm. The interrogation width area was set at 64 px with a step of 32 px for the first pass, and a width of 32 px with a step of 16 px for a second pass. A Gauss 2×3 point for the sub-pixel estimator and a standard correlation robustness setting were applied. Similar settings were applied for the experimental radiographs, with the addition of a CLAHE filter of 64 px during image preprocessing. For the side detector analysis, a mask drawn at the free surface of the side view detector (1) was implemented to ignore all displacements above the free surface. Obtained displacements for detector 1 were calibrated using height h_2 and for detector 2 using the known flume width. The final results were averaged in time with no additional filtering.

Data availability

The data supporting the figures are provided in the Supplementary Source Data file in excel format. Source data are provided with this paper.

Code availability

The open source code developed for estimating the free surface using two orthogonal x-rays has been added as part of the *PynamiX* toolset, available at: <https://github.com/scigem/PynamiX>.

References

- Lunkenheimer, P., Loidl, A., Riechers, B., Zaccone, A. & Samwer, K. Thermal expansion and the glass transition. *Nat. Phys.* **19**, 694–699 (2023).
- Xie, R. et al. Glass transition temperature from the chemical structure of conjugated polymers. *Nat. Commun.* **11**, 893 (2020).
- Goyon, J., Colin, A., Ovarlez, G., Ajdari, A. & Bocquet, L. Spatial cooperativity in soft glassy flows. *Nature* **454**, 84–87 (2008).
- Kim, S. & Kamrin, K. A second-order non-local model for granular flows. *Front. Phys.* **11**, 1092233 (2023).
- Pouliquen, O., Delour, J. & Savage, S. B. Fingering in granular flows. *Nature* **386**, 816–817 (1997).
- Börzsönyi, T., Ecke, R. E. & McElwaine, J. N. Patterns in flowing sand: understanding the physics of granular flow. *Phys. Rev. Lett.* **103**, 178302 (2009).
- Brodu, N., Delannay, R., Valance, A. & Richard, P. New patterns in high-speed granular flows. *J. Fluid Mech.* **769**, 218–228 (2015).
- Einstein, H. A. & Li, H. Secondary currents in straight channels. *Eos Trans. Am. Geophys. Union* **39**, 1085–1088 (1958).
- Nezu, I. & Nakagawa, H. Cellular secondary currents in straight conduit. *J. Hydraul. Eng.* **110**, 173–193 (1984).
- Tamburrino, A. & Gulliver, J. S. Free-surface visualization of streamwise vortices in a channel flow. *Water Resources Res.* **43**, 5988 (2007).
- Grega, L. M., Hsu, T. Y. & Wei, T. Vorticity transport in a corner formed by a solid wall and a free surface. *J. Fluid Mech.* **465**, 331–352 (2002).
- Mulligan, S., De Cesare, G., Casserly, J. & Sherlock, R. Understanding turbulent free-surface vortex flows using a Taylor-Couette flow analogy. *Sci. Rep.* **8**, 824 (2018).
- Naot, D. & Rodi, W. Calculation of secondary currents in channel flow. *J. Hydraul. Div.* **108**, 948–968 (1982).
- Pavlovskii, D. Secondary flows in a layer with a free surface. *Fluid Dyn.* **29**, 661–673 (1994).

15. Yang, S.-Q., Tan, S. K. & Wang, X.-K. Mechanism of secondary currents in open channel flows. *J. Geophys. Res. Earth Surf.* **117**, 2510 (2012).
16. Blanckaert, K. & De Vriend, H. J. Secondary flow in sharp open-channel bends. *J. Fluid Mech.* **498**, 353–380 (2004).
17. Zampiron, A., Cameron, S. & Nikora, V. Secondary currents and very-large-scale motions in open-channel flow over streamwise ridges. *J. Fluid Mech.* **887**, A17 (2020).
18. Bathurst, J. C., Thorne, C. R. & Hey, R. D. Direct measurements of secondary currents in river bends. *Nature* **269**, 504–506 (1977).
19. Nikora, V. & Roy, A. G. *Secondary Flows in Rivers: Theoretical Framework, Recent Advances, and Current Challenges*, chap. 1, 1–22 (Wiley, 2012).
20. Forterre, Y. & Pouliquen, O. Longitudinal vortices in granular flows. *Phys. Rev. Lett.* **86**, 5886 (2001).
21. Forterre, Y. & Pouliquen, O. Stability analysis of rapid granular chute flows: formation of longitudinal vortices. *J. Fluid Mech.* **467**, 361–387 (2002).
22. Rognon, P. G., Miller, T., Metzger, B. & Einav, I. Long-range wall perturbations in dense granular flows. *J. Fluid Mech.* **764**, 171–192 (2015).
23. Guillard, F., Marks, B. & Einav, I. Dynamic x-ray radiography reveals particle size and shape orientation fields during granular flow. *Sci. Rep.* **7**, 8155 (2017).
24. Zade, S., Shamu, T. J., Lundell, F. & Brandt, L. Finite-size spherical particles in a square duct flow of an elastoviscoplastic fluid: an experimental study. *J. Fluid Mech.* **883**, A6 (2020).
25. Ramachandran, A. & Leighton, D. T. The influence of secondary flows induced by normal stress differences on the shear-induced migration of particles in concentrated suspensions. *J. Fluid Mech.* **603**, 207–243 (2008).
26. Mueth, D. et al. Signatures of granular microstructure in dense shear flows. *Nature* **406**, 385–389 (2000).
27. Wortel, G. et al. Heaping, secondary flows and broken symmetry in flows of elongated granular particles. *Soft Matter* **11**, 2570–2576 (2015).
28. Tengattini, A., Nguyen, G. D., Viggiani, G. & Einav, I. Micro-mechanically inspired investigation of cemented granular materials: part ii—from experiments to modelling and back. *Acta Geotechnica* **18**, 57–75 (2023).
29. Barés, J. et al. Compacting an assembly of soft balls far beyond the jammed state: Insights from three-dimensional imaging. *Phys. Rev. E* **108**, 044901 (2023).
30. Mohammadi, M., Puzyrev, D., Trittel, T. & Stannarius, R. Secondary flow in ensembles of nonconvex granular particles under shear. *Phys. Rev. E* **106**, L052901 (2022).
31. Stannarius, R., Fischer, D. & Börzsönyi, T. Heaping and secondary flows in sheared granular materials. *EPJ Web Conf.* **140**, 03025 (2017).
32. Krishnaraj, K. & Nott, P. R. A dilation-driven vortex flow in sheared granular materials explains a rheometric anomaly. *Nat. Commun.* **7**, 10630 (2016).
33. Conway, S. L., Shinbrot, T. & Glasser, B. J. A Taylor vortex analogy in granular flows. *Nature* **431**, 433–437 (2004).
34. Cabrera, M. & Polanía, O. Heaps of sand inflows within a split-bottom couette cell. *Phys. Rev. E* **102**, 062901 (2020).
35. Charru, F., Mouilleron, H. & Eiff, O. Erosion and deposition of particles on a bed sheared by a viscous flow. *J. Fluid Mech.* **519**, 55–80 (2004).
36. Zheng, Q., Luo, Q. & Yu, A. Continuum modelling of primary and secondary granular flows in a torsional shear cell. *Powder Technol.* **361**, 10–20 (2020).
37. Sauret, A., Balmforth, N., Caulfield, C. & McElwaine, J. Bulldozing of granular material. *J. Fluid Mech.* **748**, 143–174 (2014).
38. Gravish, N., Umbanhowar, P. B. & Goldman, D. I. Force and flow at the onset of drag in plowed granular media. *Phys. Rev. E* **89**, 042202 (2014).
39. Hegde, A. & Murthy, T. G. Experimental studies on deformation of granular materials during orthogonal cutting. *Granul. Matter* **24**, 70 (2022).
40. Baker, J., Guillard, F., Marks, B. & Einav, I. X-ray rheography uncovers planar granular flows despite non-planar walls. *Nat. Commun.* **9**, 5119 (2018).
41. Dsouza, P. V. & Nott, P. R. Dilatancy-driven secondary flows in dense granular materials. *J. Fluid Mech.* **914**, A36 (2021).
42. Baker, J. L. & Einav, I. Deep velocimetry: Extracting full velocity distributions from projected images of flowing media. *Exp. Fluids* **62**, 102 (2021).
43. Savage, S. B. & Hutter, K. The motion of a finite mass of granular material down a rough incline. *J. fluid Mech.* **199**, 177–215 (1989).
44. Gray, J., Wieland, M. & Hutter, K. Gravity-driven free surface flow of granular avalanches over complex basal topography. *Proc. R. Soc. Lond. Ser. A: Math. Phys. Eng. Sci.* **455**, 1841–1874 (1999).
45. Pastor, M. et al. Depth averaged models for fast landslide propagation: mathematical, rheological and numerical aspects. *Arch. Comput. Methods Eng.* **22**, 67–104 (2015).
46. Magnarini, G., Mitchell, T. M., Grindrod, P. M., Goren, L. & Schmitt, H. H. Longitudinal ridges imparted by high-speed granular flow mechanisms in martian landslides. *Nat. Commun.* **10**, 4711 (2019).
47. Krinitzsky, E. L. *Radiography in the Earth Sciences and Soil Mechanics* (Springer, 2012).
48. Smilauer, V. et al. *Yade Documentation 3rd ed.* (The Yade Project, 2021).
49. Pournin, L., Liebling, T. M. & Mocellin, A. Molecular-dynamics force models for better control of energy dissipation in numerical simulations of dense granular media. *Phys. Rev. E* **65**, 011302 (2001).
50. Tuononen, A. J. Onset of frictional sliding of rubber–glass contact under dry and lubricated conditions. *Sci. Rep.* **6**, 27951 (2016).
51. Hoover, W. G. & Hoover, C. G. Smooth-particle phase stability with generalized density-dependent potentials. *Phys. Rev. E* **73**, 016702 (2006).
52. Stamhuis, E. & Thielicke, W. Pivlab—towards user-friendly, affordable and accurate digital particle image velocimetry in matlab. *J. Open Res. Softw.* **2**, 30 (2014).

Acknowledgements

The authors would like to acknowledge Benjy Marks for his assistance in the experimental procedures. Special thanks also to Todd Budrodeen for developing the acrylic flume and providing essential refinements to ensure the smooth and reliable functioning of the experimental setup. A.E. and T.F. acknowledge support from LabEx OSUG@2020 (Investissements d’avenir - ANR10 LABX56) and PHC FASIC 2022 programme (France-Australia funding). I.E. acknowledges support from the Australian Research Council (Grant Number LE250100091).

Author contributions

A.E. developed the experimental setup, performed the experiments, and developed the simulations. A.E., J.B., F.G., T.F. and I.E. took part in the design of the setup and experiments, and participated in writing the manuscript. The experiment’s velocity reconstruction algorithm was previously developed by J.B., F.G. and I.E. in conjunction with Benjy Marks. J.B. initially implemented this algorithm for the conveyor belt setup before A.E. explored different tests and parameters.

Competing interests

The authors declare no competing interests.

Additional information

Supplementary information The online version contains supplementary material available at <https://doi.org/10.1038/s41467-025-62669-y>.

Correspondence and requests for materials should be addressed to Itai Einav.

Peer review information *Nature Communications* thanks the anonymous reviewers for their contribution to the peer review of this work. A peer review file is available.

Reprints and permissions information is available at <http://www.nature.com/reprints>

Publisher's note Springer Nature remains neutral with regard to jurisdictional claims in published maps and institutional affiliations.

Open Access This article is licensed under a Creative Commons Attribution-NonCommercial-NoDerivatives 4.0 International License, which permits any non-commercial use, sharing, distribution and reproduction in any medium or format, as long as you give appropriate credit to the original author(s) and the source, provide a link to the Creative Commons licence, and indicate if you modified the licensed material. You do not have permission under this licence to share adapted material derived from this article or parts of it. The images or other third party material in this article are included in the article's Creative Commons licence, unless indicated otherwise in a credit line to the material. If material is not included in the article's Creative Commons licence and your intended use is not permitted by statutory regulation or exceeds the permitted use, you will need to obtain permission directly from the copyright holder. To view a copy of this licence, visit <http://creativecommons.org/licenses/by-nc-nd/4.0/>.

© The Author(s) 2025